ELSEVIER

Journal of Organometallic Chemistry 573 (1999) 121–133

Journal of Organometallic Chemistry

Remarkably stable radical anions derived from clusters $[HOs_3(CO)_9(L)]$, L = *ortho*-metallated α-diimine: a spectro-electrochemical study and theoretical rationalization[1]

J. Nijhoff [a], F. Hartl [a,*], J.W.M. van Outersterp [a], D.J. Stufkens [a], M.J. Calhorda [b], L.F. Veiros [c]

[a] *Anorganisch Chemisch Laboratorium, Institute of Molecular Chemistry, Universiteit van Amsterdam, Nieuwe Achtergracht 166, 1018 WV Amsterdam, The Netherlands*

[b] *ITQB, R. da Quinta Grande, 6, Apart. 127, 2780 Oeiras, and Dept. Química e Bioquímica, FCUL, 1700 Lisboa, Portugal*

[c] *Centro de Química Estrutural, IST, Av. Rovisco Pais, 1096 Lisboa Codex, Portugal*

Received 25 March 1998

Abstract

Reduction of the cluster $[Os_3(CO)_{10}(^i$Pr-PyCa)], ^{i}Pr–PyCa = σ-*N*,σ-*N*′-pyridine-2-carbaldehyde-*N*-isopropyl-imine, (**1**) follows an ECEC sequence. The initial one-electron reduction step produces the radical anion $\mathbf{1}^{-\bullet}$ which was found stable on a subsecond time scale at low temperatures. At room temperature an open-structure radical anionic transient $\mathbf{1a}^{-\bullet}$ is formed which instantaneously reduces to $\mathbf{1a}^{2-}$. Subsequent attack of the latter species at yet nonreduced **1** yields an Os–Os bonded cluster dimer $[\mathbf{1a}–\mathbf{1a}]^{2-}$. In contrast to the reactivity of $\mathbf{1}^{-\bullet}$, the radical anions of the clusters $[HOs_3(CO)_9(C_5H_3N$-2-C(H)=N–^{i}Pr)] (**2**), $[HOs_3(CO)_9(6$-CH_2–C_5H_3N-2-C(H)=N–^{i}Pr)] (**3**), containing the *ortho*-metallated ligands *o*-^{i}Pr–PyCa{6-X} (X = H, Me}, are substantially more stable. At room temperature in THF, $\mathbf{2}^{-\bullet}$ and $\mathbf{3}^{-\bullet}$ slowly disproportionate to moderately stable dianionic species **2b** and **3c**. IR and ^{1}H-NMR spectra of **2b** have revealed the presence of bridging CO and terminal hydride ligands, and the dominant localization of the negative charge on the metallic core. The structure of **3c** is probably similar. The latter dianions were also obtained by direct one-electron reduction of $\mathbf{2}^{-\bullet}$ and $\mathbf{3}^{-\bullet}$, respectively. Both radical anions are inherently stable at $T = 253$ K. According to extended Hückel molecular orbital calculations on models of the parent clusters **1**–**3**, the higher stability of $\mathbf{2}^{-\bullet}$ and $\mathbf{3}^{-\bullet}$ relative to that of $\mathbf{1}^{-\bullet}$ has its origin in larger localization of the odd electron at the lowest π*-orbital of the *ortho*-metallated ligands compared to the σ*N*,σ*N*′-chelated ^{i}Pr–PyCa ligand, and in higher cluster-diimine binding energies of **2** and **3** which drop due the one-electron reduction less than calculated for the couple $\mathbf{1}/\mathbf{1}^{-\bullet}$. IR and ^{1}H-NMR spectra have revealed that 2,3-dipyrid-2′-ylbenzoquinoxaline (dpb) coordinates to the Os_3 core as an *ortho*-metallated ligand, forming $[HOs_3(CO)_9$(dpb-14-yl)] (**4**), in contrast to shorter 2,3-dipyrid-2′-ylpyrazine (dpp). The corresponding radical anion $\mathbf{4}^{-\bullet}$ is inherently stable already at room temperature, mainly due to the large π-acceptor capacity of the *ortho*-metallated dpb ligand.

Keywords: Osmium clusters; α-Diimine complexes; Radical anions; Spectroelectrochemistry; Cyclic voltammetry; Extended Hückel calculations

1. Introduction

The large synthetic versatility of carbonyl triosmium clusters makes them one of the most frequently studied compounds in the field of cluster chemistry [1]. Increasing attention is being devoted to their photochemical

* Corresponding author. Tel.: +31 20 5256450; fax: +31 20 5256456; e-mail: hartl@anorg.chem.uva.nl

[1] Dedicated to Professor Brian F.G. Johnson, FRS on the occasion of his 60th birthday in recognition of his outstanding contributions to the chemistry of transition metal clusters.

0022-328X/99/$ - see front matter
PII S0022-328X(98)00831-6

and redox activation via Os–Os bond cleavage or ligand dissociation, creating one or more vacant coordination sites. The selectivity of these processes offers great opportunities for binding and activation of organic substrates [2]. Promising candidates for such studies are triosmium clusters containing nitrogen heterocycles as ligands [3], some of them being reported as potentially efficient catalysts for industrial synthetic applications [4].

Our systematic investigations of the photochemistry and electrochemical reduction of the clusters $[Os_3(CO)_{10}(\alpha\text{-diimine})]$ led to description of a variety of biradical, zwitterionic, radical anionic and dianionic open-structure intermediates and products resulting from electron-transfer-induced cleavage of an Os–Os(α-diimine) bond [5,6]. In this respect the clusters $[Os_3(CO)_{10}(\alpha\text{-diimine})]$ strongly resemble the bimetallic complexes $[(CO)_5Mn-Mn(CO)_3(\alpha\text{-diimine})]$ [7], with the special property, that the remaining Os–Os bonds hold the radical and anionic fragments together. The reduction path of $[Os_3(CO)_{10}(\alpha\text{-diimine})]$ with σ-donor α-diimine ligands [6] also bears striking resemblance to the ECEC reduction path of the complexes $[Mn(X)(CO)_3(\alpha\text{-diimine})]$ [8]. The primary one-electron reduction step affords the radical anions $[Os_3(CO)_{10}(\alpha\text{-diimine})]^{-\bullet}$ whose stability towards the Os–Os bond cleavage is substantially higher compared to the very shortly lived unsubstituted $[Os_3(CO)_{12}]^{-\bullet}$ species [9], pointing to the stabilizing role of the π-acceptor α-diimine ligand as the redox active centre.

The goal of this article is to find out whether a higher stability of the triosmium radical anions can be achieved on coordination of the α-diimine ligand to more than one Os centre. Attention is focused on the triangular clusters $[HOs_3(CO)_9(L)]$, L = *ortho*-metallated 6-X-pyridine-2-carbaldehyde-*N*-isopropyl-imine (*o*-^{i}Pr–PyCa{6-X}; X = H (**2**), Me (**3**)), and 2,3-dipyrid-2′-ylbenzoquinoxaline-14-yl (dpb-14-yl) (**4**). The cluster $[Os_3(CO)_{10}(^i\text{Pr–PyCa})]$ (**1**) was chosen as a suitable reference compound. The molecular structures of **1**–**4** are schematically depicted in Fig. 1.

2. Experimental section

2.1. Materials and preparations

$Os_3(CO)_{12}$ (ABCR), pyridine-2-carboxaldehyde, 6-methylpyridine-2-carboxaldehyde and isopropylamine (all Janssen), ferrocene (Fc, BDH) and cobaltocene ($CoCp_2$, Aldrich) were used as received. $[Fe^I(Cp)(C_6Me_6)]$ [10] and the α-diimine ligands pyridine-2-carbaldehyde-*N*-isopropyl-imine (^{i}Pr–PyCa) [11], 6-methyl-pyridine-2-carbaldehyde-*N*-isopropyl-imine (^{i}Pr–PyCa{6-Me}) [12] and 2,3-dipyrid-2′-ylbenzoquinoxaline (dpb) [13] were prepared according the literature procedures. Syntheses of the clusters $[Os_3(CO)_{10}(^i\text{Pr–PyCa})]$ (**1**) [14], $[HOs_3(CO)_9(o\text{-}^i\text{Pr–PyCa})]$, *o*-^{i}Pr–PyCa=$C_5H_3N$-2-C(H)=N–^{i}Pr, (**2**) [14], $[HOs_3(CO)_9(o\text{-}^i\text{Pr–PyCa\{6-Me\}})]$, *o*-^{i}Pr–PyCa{6-Me}=6-CH_2–C_5H_3N-2-C(H)=N–^{i}Pr, (**3**) [15] and $[HOs_3(CO)_9(\text{dpb-14-yl})]$ (**4**) (assigned in the literature as '$Os_3(CO)_{10}$(dpb)') [5] have been described in the literature. Solvents for synthetic purposes (reagent grade) and for (spectro)electrochemical experiments (spectroscopic grade), all purchased from Janssen, were freshly distilled under nitrogen from a benzophenone–sodium mixture (THF), sodium wire (hexane, 1,2-dimethoxy-ethane (DME)) and CaH_2 (acetonitrile (MeCN), butyronitrile (^{n}PrCN)). Silicagel (Kieselgel 60, Merck) for column chromatography was dried and activated by heating overnight in vacuo at 160°C. The supporting electrolyte Bu_4NPF_6 (Aldrich) was recrystallized twice from absolute EtOH and dried in vacuo at 80°C for 10 h.

2.2. Spectroscopic measurements

UV-vis absorption spectra were recorded on software-updated Perkin-Elmer Lambda 5 or Varian Cary 4E spectrophotometers. FTIR measurements were carried out using Bio-Rad FTS 7 or FTS-60A spectrometers. ^{1}H-NMR measurements were obtained with a Bruker AMX 300 spectrometer, and X-band EPR spectra with a Varian Century E-104A spectrometer. EPR *g*-values were determined relative to the 2,2′-diphenyl-1-picrylhydrazyl radical (DPPH, Aldrich) as an external '*g*-mark' ($g = 2.0037$).

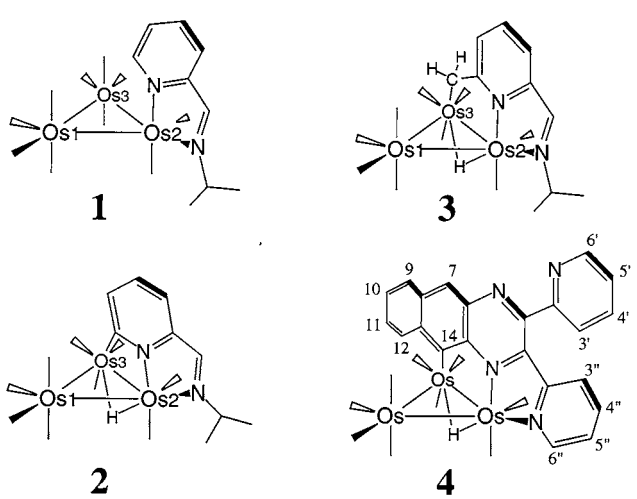

Fig. 1. Structures of the clusters $[Os_3(CO)_{10}(^i\text{Pr–PyCa})]$ (**1**), $[HOs_3(CO)_9(C_5H_3N\text{-}2\text{-}C(H)=N-^i\text{Pr})]$ (**2**), $[HOs_3(CO)_9(6\text{-}CH_2-C_5H_3N\text{-}2\text{-}C(H)=N-^i\text{Pr})]$ (**3**) and $[HOs_3(CO)_9(2,3\text{-dipyrid-2′-ylbenzoquinoxaline-14-yl})]$ (**4**).

2.3. Cyclic voltammetry and spectroelectrochemistry

Cyclic voltammetry was carried out with a PAR Model 283 potentiostat on a carefully polished Pt disk electrode (0.42 mm^2 apparent surface area) placed in a gastight three-electrode cell. Pt gauze and a coiled Ag wire were employed as auxiliary and pseudoreference electrodes, respectively. All redox potentials are reported against the ferrocene/ferrocenium (Fc/Fc^+) redox couple ($E_{1/2} = +0.575$ V versus SCE in THF) used as an internal standard [16]. The apparent number of electrons transferred during reduction of the parent clusters on the time scale of cyclic voltammetry (n_{app}) was determined as described in the literature [8,17]. IR and UV-vis spectroelectrochemical experiments at room and low temperatures were performed with previously described OTTLE cells [18,19] equipped with a Pt minigrid working electrode (32 wires/cm) and quartz or $NaCl/CaF_2$ optical windows. EPR spectra of the electrogenerated radicals were recorded at variable temperatures using a modified three-electrode Allendoerfer-type [20] spectroelectrochemical cell equipped with a single-point Ag pseudoreference electrode [21]. Thin-layer cyclic voltammograms were recorded in the course of the spectroelectrochemical experiments. The potential control was achieved by a PA4 potentiostat (EKOM, Czech Republic). Bu_4NPF_6 (3×10^{-1} M) was used as the supporting electrolyte in all (spectro)electrochemical experiments. The concentration of the studied clusters was typically 10^{-3} M for cyclic voltammetry and EPR spectroelectrochemistry, and 10^{-2} M for UV-vis/IR spectroelectrochemistry.

2.4. Molecular orbital calculations

All the calculations were performed using the extended Hückel method [22] with modified H_{ij} values [23]. The basis set for the metal atoms consisted of *n*s, *n*p and $(n-1)$d orbitals. The s and p orbitals were described by single Slater-type wave functions, and the d orbitals were taken as contracted linear combinations of two Slater-type wave functions. The parameters used for Os were (H_{ii} (eV), ζ): 6s −8.17, 2.452; 6p −4.81, 2.429; 5d −11.84, 5.571, 2.416 (ζ_2), 0.6372 (C_1), 0.5598 (C_2). Standard parameters were used for other atoms. Three-dimensional representations of the frontier orbitals were drawn using the program CACAO [24].

The clusters **2** and **3** were studied using the corresponding crystal structures [14,15], with the ^{i}Pr-groups replaced by H atoms. For the cluster **1** a model compound with idealised geometry was created. This was based on the crystal structure of $[Os_3(CO)_{10}(^iPr–DAB)]$ (^{i}Pr–DAB = 1,4-diisopropyl-1,4-diaza-1,3-butadiene) [25]. The bond distances (Å) were as follows: Os–Os, 2.90; Os–C (CO), 1.95; Os–N, 2.15; Os–C, 2.15; Os–H, 1.80; C–O, 1.15; C–N, 1.40; C–C, 1.40; C–H, 1.08; N–H, 1.08.

3. Results and discussion

The redox potentials, IR ν(CO) wavenumbers and UV-vis absorption maxima of the triosmium clusters **1-4** and their reduction products under study (denoted by boldface numbers as defined in the text) are summarized in Tables 1–3, respectively.

3.1. Redox behaviour of $[Os_3(CO)_{10}(^iPr\text{-}PyCa]$ (1)

The structure proposed by Zoet et al. for **1** with the 4e donor ^{i}Pr-PyCa ligand coordinating perpendicularly to the triosmium plane, and the pyridine ring occupying the axial position [14] (see Fig. 1(**1**)), was indeed found to be most stable according to density functional MO calculations [26]. The total energies of the alternative isomeric structures where (i) the axial position is occupied by the imino nitrogen atom, or (ii) the ^{i}Pr–PyCa ligand lies in the equatorial plane, have been found higher by 0.180 and 0.313 eV, respectively. The solid state molecular structure of **1** is thus assumed to resemble closely those reported for the derivatives $[Os_3(CO)_{10}(L)]$ (L = 2,2′-bipyridine (bpy) [27] and ^{i}Pr–DAB [25]).

The π-acceptor capacity of the ^{i}Pr–PyCa ligand is known to be slightly larger than that of 2,2′-bipyridine [28]. This property is reflected in the more positive reduction potential of **1** (see Table 1) compared to the value for $[Os_3(CO)_{10}(bpy)]$ ($E_{p,c} = -1.85$ V in THF at 293 K) [6]. Apparently, the LUMO of **1** possesses a prevailing contribution from the lowest $\pi^*(^iPr–PyCa)$ orbital, which agrees with results of a resonance Raman study ([5]b) and extended Hückel calculations (see below). The HOMO is then more localized on the triosmium core. On the basis of the similar electronic structure of $[Os_3(CO)_{10}(L)]$ (L = bpy, ^{i}Pr–PyCa) we expected little difference in their redox behaviour. The cyclic voltammograms of **1** recorded in THF at 293 and 220 K are depicted in Fig. 2A and B, respectively.

Identical to $[Os_3(CO)_{10}(bpy)]$ [6], reduction of the ^{i}Pr–PyCa derivative in THF at room temperature is chemically irreversible (cathodic peak R_1) and corresponds at $v = 100$ mV s^{-1} to an overall transfer of two electrons ($n_{app} = 1.92$). Scan reversal behind R_1 shows two anodic peaks O_2^* and O_2^{**} which are assigned in accordance with the results for $[Os_3(CO)_{10}(bpy)]$ [6] to the oxidation of the short-lived open-structure dianion $[(CO)_4Os^- –Os(CO)_4–Os^-(CO)_2(^iPr–PyCa)]^{2-}$ ($\mathbf{1a}^{2-}$) and the dimer $[(CO)_4Os^- –Os(CO)_4–Os(CO)_2(^iPr–PyCa)]_2^{2-}$ ($[\mathbf{1a}–\mathbf{1a}]^{2-}$) with an (^{i}Pr–PyCa)Os–Os(^{i}Pr–PyCa) bond, respectively (see Scheme 1 and Table 1). The reduced cluster $\mathbf{1a}^{2-}$ is structurally related to the solvent-stabilized open-structure zwitterion $[(CO)_4Os^- –Os(CO)_4–Os^+(Sv)(CO)_2(^iPr–PyCa)]$ ($\mathbf{1a}\cdot Sv$), the known photoproduct of **1** in donor solvents ([5]b). On cooling to 220 K the reduction of **1** at

Table 1
Redox potentials of the clusters **1**–**4** and their reduction products[a]

Cluster[b]	$E_{p,c}$ (V)[d]	ΔE_p (mV)	$E_{p,a}$ (V)[d]	ΔE_p (mV)	ΔE_p (mV) (Fc/Fc$^+$)
1	−1.77 (irr, 2e)		+0.20 (irr, 2e)		100
1[c]	−1.73 (rev)	80	+0.31 (irr, 2e)		80
1$^{-\bullet}$[c]	−2.23 (irr, 1e)	320			80
[**1a**–**1a**]$^{2-}$			−0.75 (irr)		
[**1a**–**1a**]$^{2-}$[c]			−0.66 (irr)		
1a^{2-}			−1.43 (irr, 2e)		
1a^{2-}[c]			−1.31 (irr, 2e)		
1a·CO	−1.56 (irr)				
2	−1.76 (rev)	80	+0.58 (irr, 2e)		80
2$^{-\bullet}$	−2.20 (irr, 1e)				
2b			−1.17 (irr)		
3	−1.88 (rev)	100	+0.46 (irr, 2e)		100
3[c]	−1.83 (rev)	100	+0.47 (irr, 1e)	120	100
3$^{-\bullet}$	−2.45 (irr, 2e)				
3b			−1.19 (irr)		
3c	−2.61 (irr)		−0.52 (irr)		
4	−1.30 (rev)	80	+0.52 (irr, 2e)		80
4$^{-\bullet}$	−2.03 (irr)	125			80

[a] Conditions and definitions: 10^{-3} M solutions in THF (containing 3×10^{-1} M Bu_4NPF_6) at $T = 293$ K unless stated otherwise; Pt disk electrode; $v = 100$ mV s^{-1}; redox potentials versus $E_{1/2}$ (Fc/Fc$^+$): $E_{p,c}$, cathodic peak potential for reduction of parent cluster or its radical anion; $E_{p,a}$, anodic peak potential for oxidation of parent cluster or its reduction products; ΔE_p, peak separation for a redox couple.
[b] Assignment given in the text.
[c] $T = 220$ K.
[d] Chemical reversibility and irreversibility denoted by (rev) and (irr), respectively.

$E(R_1)$ turns to a chemically and electrochemically reversible ($v = 100$ mV s^{-1}) one-electron process (see Fig. 2B). This step yields the corresponding radical anion **1**$^{-\bullet}$. The cathodic peak R_2 in Fig. 2B then belongs to the subsequent chemically irreversible one-electron reduction of **1**$^{-\bullet}$ which again produces the open-structure dianion **1a**$^{2-}$ identified on the reverse anodic scan due to its oxidation at the potential $E(O_2^*)$.

Cyclic voltammetry thus documents that **1**$^{-\bullet}$ is very unstable at 293 K and readily transforms to the open-structure dianion **1a**$^{2-}$, probably via the open-structure radical transient [$(CO)_4Os^- – Os(CO)_4 – Os^+(CO)_2$(^{i}Pr–PyCa$^{-\bullet}$)] (**1a**$^{-\bullet}$) which is further reduced directly at the electrode potential $E(R_1)$ to **1a**$^{2-}$. The latter dianionic product was, however, not observed in the course of the reduction of **1** at 293 K, followed in situ by IR spectroscopy on the timescale of seconds. Instead, the only observable product was the cluster dimer [**1a**–**1a**]$^{2-}$ (see Table 2). The dimer was also formed by reducing **1** with one molar equivalent of [Fe^I(Cp)(C_6Me_6)]. Its formation can be explained by a rapid nucleophilic attack of the two-electron-reduced cluster **1a**$^{2-}$ at the parent cluster **1** (see Scheme 1). This process can be inhibited at sufficiently low temperatures [6]. Notably, a similar concerted zero-electron coupling reaction is known to occur between mononuclear complexes [Mn(Sv)$(CO)_3$(L)]$^+$ and two-electron-reduced [Mn$(CO)_3$(L)]$^-$ (Sv = THF, MeCN; L = bpy, ^{i}Pr–DAB), producing the dimers [Mn$(CO)_3$(L)]$_2$ [8].

The back oxidation of **1a**$^{2-}$ at the anodic potential $E(O_2^*)$ (see Fig. 2) is probably a two-electron process [6,8], yielding initially the zwitterion **1a** (see Scheme 1). The latter species reacts rapidly further with yet unoxidized **1a**$^{2-}$ to produce ultimately [**1a**–**1a**]$^{2-}$ which oxidizes more positively at $E(O_2^{**})$. Evidence for this route has been obtained from recording the cyclic voltammogram of **1** in CO-saturated THF at 293 K (not shown in Fig. 2). The negative scan reversal beyond the anodic peak O_2^* due to the oxidation of **1a**$^{2-}$ revealed a new cathodic peak at $E_{p,c} = 1.56$ V which probably belongs to the reduction of the zwitterion **1a** stabilized by coordination of CO at the coordinatively unsaturated $Os^+(CO)_2$(^{i}Pr–PyCa) site, i.e. **1a**·CO [6]. As expected, this cathodic peak was not recorded in N_2-saturated THF where corresponding **1a**·THF is detectable at room temperature only on a submicrosecond time scale ($\tau = 204$ ns) ([5]b). Contrary to this, **1a**·CO is considerably more stable [29]. The oxidation path of **1a**$^{2-}$ again closely resembles that of [Mn$(CO)_3$(L)]$^-$ (L = bpy, ^{i}Pr–DAB) [8]. This similarity arises from the fact that also in **1** and **1a**$^{2-}$ the redox-active centre is the Os$(CO)_2$(L) site.

Oxidation of **1** at the potential $E(O_m)$ is chemically irreversible and consumes more than one electron (see Fig. 2A). IR spectroelectrochemical experiments

showed formation of a single carbonyl product (ν(CO) at 2132w, 2085m, 2050s, 2012s, 2004s, 1988s, 1950w and 1938w cm^{-1}) whose back reduction at $E(R'_m)$ did not recover **1**. Similar products were obtained on oxidation of other $[Os_3(CO)_{10}(L)]$ clusters, e.g. for L = more basic 2,2′-bipyridine and less basic 2,2′-bipyrimidine, showing the same ν(CO) band pattern and α-diimine-dependent ν(CO) wavenumbers [6]. Research is in progress to assign these oxidized cluster species.

3.2. Redox behaviour of $[HOs_3(CO)_9(C_5H_3N\text{-}2\text{-}C(H)=N\text{-}^iPr)]$ (2)

The UV-vis spectra of the clusters **2** (Fig. 1(**2**)) and **3** (Fig. 1(**3**)) with the *o*-^{i}Pr–PyCa and *o*-^{i}Pr–PyCa{6-Me} ligands, respectively, exhibit several absorption bands in the near-UV-vis region (see Table 3). The two absorption bands in the visible region are strongly solvatochromic and shift to a higher energy with increasing polarity of the solvent, while the absorption maxima of the higher lying bands are nearly solvent independent. The negative solvatochromism of the visible absorption bands points to an OsL charge transfer (MLCT) nature of the corresponding electronic transitions. The LUMO of both **2** and **3** will therefore be largely localized on the *ortho*-metallated α-diimine ligand, as was also found for the $\sigma N,\sigma N'$-coordinated ^{i}Pr–PyCa ligand in **1**.

The cyclic voltammogram of **2** in THF at 293 K is shown in Fig. 3. Although the reduction potentials of **1** and **2** are nearly identical (see Table 1), the reduction of **2** at $E(R_1)$ is chemically reversible at moderate scan rates already at room temperature (the peak-current ratio $I_{p,a}(O_1)/I_{p,c}(R_1) = 1$). Identical with the reduction of **1** at 220 K, the latter process is an one-electron step which affords the corresponding radical anion $\mathbf{2}^{-\bullet}$. Subsequent one-electron reduction of $\mathbf{2}^{-\bullet}$ at the potential $E(R_2)$ is chemically irreversible. It yields a cluster denoted as **2b**, which is oxidized on the reverse anodic scan at the potential $E(O'_2)$. The molecular structure of **2b** is discussed hereinafter. Oxidation of **2** at $E(O_m)$ is a chemically irreversible process which corresponds at $v = 100$ mV s^{-1} to the transfer of two electrons, as evidenced by the peak-current ratio $I_p(O_m)/I_p(R_1) \sim 2$ (see Fig. 3). No apparent deviation from this ratio was observed on cooling the solution to 220 K.

As proven by cyclic voltammetry, the radical anion $\mathbf{2}^{-\bullet}$ is considerably more stable than related $\mathbf{1}^{-\bullet}$. IR OTTLE studies revealed that $\mathbf{2}^{-\bullet}$ is characterized by a nearly identical intensity pattern and lower wavenumbers of its IR ν(CO) bands compared to those of the

Table 2
IR ν(CO) wavenumbers (cm^{-1}) of the clusters 1–4 and their reduction products

1[a]	2084m, 2033s, 2003vs, 1993s, 1976s, 1958m, 1907w
[1a–1a]$^{2-}$ [a]	2069vw, 2056w, 2010w, 1996sh,w, 1976vs, 1954s, 1932sh, 1907w, 1882m–w, 1868m, 1855sh
2[a,b]	2082m, 2041s, 2004vs, 1987m, 1977sh, 1958m, 1935w
2[c]	2083m, 2043s, 2005vs, 1989m, 1977sh, 1959m–w, 1932w
$2^{-\bullet}$ [a,b]	2057m, 2017s, 1981vs, 1961m, 1939w, 1927w, 1895w
$2^{-\bullet}$ [c]	2057m, 2019s, 1982vs, 1961m, 1928w, 1893w
2b[a,b]	2001m, 1970w,sh, 1946s, 1924s, 1915s, 1892sh, 1878m, 1865sh, 1843sh, 1655w
2b[c]	2002m, 1967m, 1949vs, 1922s, 1912vs, 1884s–m, 1864m, 1842sh, 1664w
2b[d]	2009m, 1980m–w, 1955s, 1928vs, 1894m, 1855m 1629w
2b[e]	2004m, 1968w,sh, 1949s, 1925vs, 1891sh, 1879m, 1866sh, 1842sh, 1655w
2b[f]	2006m, 1981m–w, 1955s, 1926vs, 1892m, 1872sh, 1845w, 1625w
3[a,b]	2074m, 2028s–m, 2005vs, 1985m, 1964m–w, 1947m–w 1937sh
$3^{-\bullet}$ [a,b]	2055m, 2009m, 1983vs, 1963m, 1943m–w, 1934sh,w, 1924m–w, 1902w
3c[a]	2026sh, 2013m–w, 1977s–m, 1943m, 1930m, 1889vs, 1881sh, 1861sh, 1807vw, 1755w, 1740w
3c[b]	2014w, 1979m, 1945sh, 1925m, 1886vs,br, 1858sh, 1799vw, 1757w, 1735w
4[g]	2078s–m, 2035s–m, 2011vs, 1988m, 1975sh, 1956w 1940sh,
$4^{-\bullet}$ [g]	2064m, 2020s–m, 1990vs, 1973s–m, 1957w, 1939w,br, 1912w
4b[g]	2036w, 1995s–m, 1952s, 1933s, 1892m, 1884m, 1663w

[a] In THF/3×10^{-1} M Bu_4NPF_6 at $T = 293$ K.
[b] In THF/3×10^{-1} M Bu_4NPF_6 at $T = 253$ K.
[c] In ^{n}PrCN/3×10^{-1} M Bu_4NPF_6 at $T = 233$ K.
[d] Na^+ salt in THF at $T = 293$ K.
[e] From the reduction of 2 with 1% Na/Hg in THF/3×10^{-1} M Bu_4NClO_4 at 293 K.
[f] From the reduction of 2 with two equivalents of $Fe^I(Cp)(C_6Me_6)$ in DME at 293 K.
[g] In ^{n}PrCN/3×10^{-1} M Bu_4NPF_6 at $T = 293$ K.

Table 3
UV-vis spectra of the clusters **2**–**4** and corresponding radical anions

Compound/solvent/temp. (K)	λ_{max} (nm)
2/MeCN/293	360sh, 398sh, 474, 540
2/THF/293	360sh, 406sh, 483, 552
2/toluene/293	360sh, 410sh, 500, 573
2/hexane/293	358, 413sh, 516, 594
2/THF[a]/253	359, 401sh, 470, 540
$\mathbf{2}^{-\bullet}$/THF[a]/253	361 (broad), 455, 561
3/MeCN/293	340sh, 410, 450sh, 520sh
3/THF/293	340sh, 409, 456, 530sh
3/toluene/293	340sh, 404, 479, 565sh
3/THF[a]/253	321sh, 401, 440, 506sh
$\mathbf{3}^{-\bullet}$/THF[a]/253	317sh, 390, 441sh, 496sh, 877(broad)
$\mathbf{4}^{-\bullet}$/^{n}PrCN[a]/293	522, 694
$\mathbf{4}^{-\bullet}$/^{n}PrCN[a]/293	510, 566, 663, 732, 819, >900
[dpb]$^{-\bullet}$[b]/THF[a]/293	490, 522, 574, 649, 711, 872(weak)

[a] Solution contained 3×10^{-1} M Bu_4NPF_6.
[b] Uncoordinated radical anion.

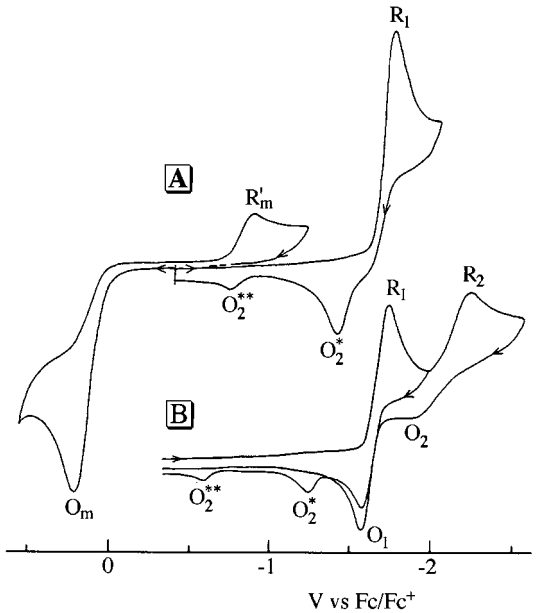

Fig. 2. Cyclic voltammograms of **1**. Conditions: THF solution of 3×10^{-1} M Bu_4NPF_6, $T = 293$ K (A) and 220 K (B), Pt disk microelectrode (0.42 mm^2 apparent surface area), $v = 100$ mV s^{-1}.

parent cluster **2** (see Fig. 4 and Table 2). The radical anion $\mathbf{2}^{-\bullet}$ remained stable in THF up to 253 K. Its EPR spectrum, recorded in THF at 243 K, shows a singlet at $g = 2.0090$ with poorly resolved hyperfine structure (see Fig. 5a).

At 293 K in THF, $\mathbf{2}^{-\bullet}$ decomposed thermally to **2b** as the only product. The radical anion was found less stable at higher concentrations. Its decomposition was also much faster in ^{n}PrCN, where it still occurred even at 233 K. In agreement with cyclic voltammetry, **2b** was also obtained by direct electrochemical reduction of the

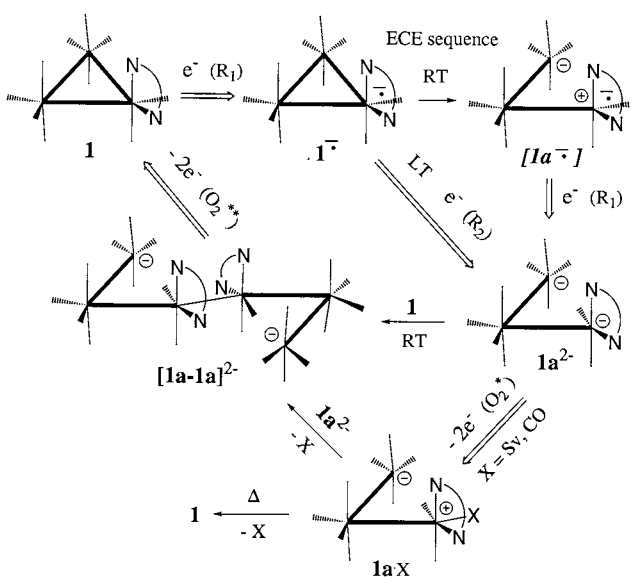

Scheme 1. The reduction path of the cluster **1** and the oxidation path of the reactive open-structure dianion $\mathbf{1a}^{2-}$. The molecular structures of the clusters are presented schematically.

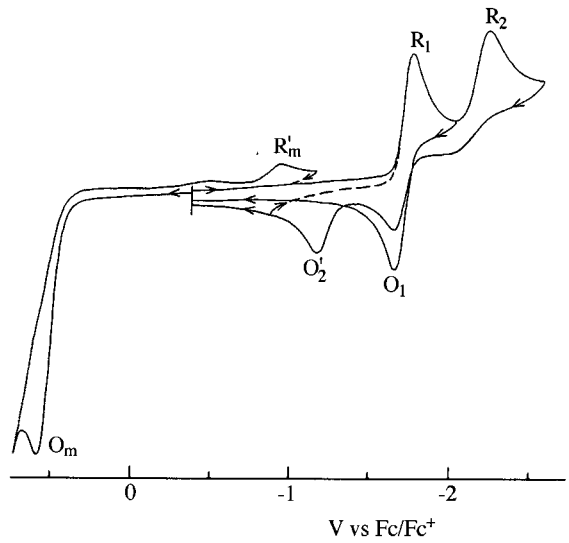

Fig. 3. Cyclic voltammogram of **2**. Conditions identical to Fig. 2A.

radical anion $\mathbf{2}^{-\bullet}$ in THF at 253 K. This result indicates that **2b** is a dianionic cluster. The IR spectrum of **2b** (see Fig. 6a and Table 2) exhibits in the ν(CO) region a diagnostically important weak band at 1655 cm^{-1} (Bu_4N^+ salt) and 1625 cm^{-1} (Na^+-salt) (see Table 2). From the IR spectra we may conclude that the cluster core of **2b** is stabilized by π-backdonation to bridging carbonyl ligand(s). This type of reactivity is common for reduced cluster carbonyls, e.g., for the two-electron-reduced tetrahedral cluster $[H_4Ru_4(CO)_{12}]^{2-}$ with edge-bridging hydride ligands, which loses a H_2 molecule and adopts a structure with three edge-bridging CO ligands [30]. From the IR spectra it was however unclear whether the hydride ligand split off completely in **2b**. The dianionic nature of **2b** was unambiguously confirmed by reducing parent **2** with $Fe^{I}(Cp)(C_6Me_6)$ ($E_{1/2}(Fe^{I/II}) = -1.99$ V versus Fc/

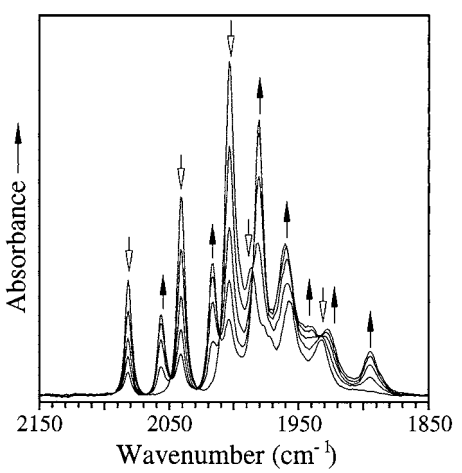

Fig. 4. Spectral changes in the IR ν(CO) region during the reduction of **2** producing the radical anion $\mathbf{2}^{-\bullet}$. Conditions: THF, $T = 253$ K, electrolysis within a low-temperature OTTLE cell [19].

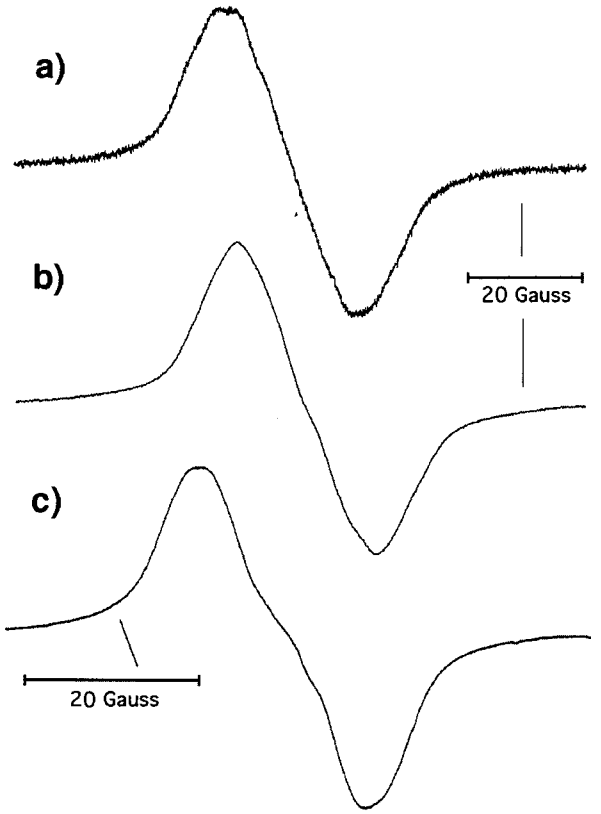

Fig. 5. EPR spectra of the radical anions (a) $\mathbf{2}^{-\bullet}$, (b) $\mathbf{3}^{-\bullet}$, and (c) $\mathbf{4}^{-\bullet}$, all in THF. Conditions: (a) in situ electrolysis within a low-temperature EPR spectroelectrochemical cell [20,21] at 243 K; (b) reduction of **3** with $[Fe^{I}(Cp)(C_6Me_6)]$ at 223 K; (c) reduction of **4** with $CoCp_2$ at 293 K.

Fc^{+}) in DME at room temperature. For, two equivalents of the one-electron reducing agent had to be added to obtain **2b** in nearly 100% yield. Notably, no $\mathbf{2}^{-\bullet}$ intermediate was detected by IR spectroscopy after addition of the first equivalent of the Fe^{I}-complex. It should be recalled that the reduction potential of the Fe^{I}-complex is too positive to accomplish the reduction of $\mathbf{2}^{-\bullet}$. This result and the relatively slow, concentration-dependent thermal reaction of $\mathbf{2}^{-\bullet}$ in less polar THF at room temperature, producing the dianion **2b** already at the applied reduction potential of **2** ($E(R_1)$), may imply a disproportionation reaction between two $\mathbf{2}^{-\bullet}$ molecules, affording **2** and **2b** which can co-exist in the solution unless **2** is further reduced. Reverse electrochemical oxidation of **2b** (Bu_4N^{+} salt) at $E(O_2')$ (see Fig. 3), followed in situ by IR spectroscopy, and oxidation of the Na^{+} and $[Fe^{II}(Cp)(C_6Me_6)]^{+}$ salts of **2b** by atmospheric oxygen led directly to the complete recovery of the parent cluster **2**.

Attempts to crystallize the dianion **2b** failed due to its slow thermal decomposition in THF or DME at room temperature to some other cluster species containing only terminal CO ligands. A valuable information about the molecular structure of **2b** could be obtained from its ^{1}H-NMR spectrum. For this purpose **2** was reduced in THF-d_8 with 1% Na/Hg and the solution was directly sealed in vacuo in an NMR tube. The ^{1}H-NMR spectrum of parent **2** in THF-d_8 was also recorded for comparison. The proton resonances of the dianion **2b** slightly shifted to lower ppm values, with the exception of the signals due to the imine proton and the bridging hydride. The former signal was found at slightly higher ppm value, while the latter shifted considerably from -20.43 to -11.66 ppm [31]. This result implies that the bridging hydride ligand of **2** did not split off during the sucessive reduction producing **2b**; instead, it probably became terminally bonded [32]. The ^{1}H-NMR data also indicate that the two added electrons in **2b** do not reside on the *ortho*-metallated ^{i}Pr–PyCa ligand. In that case, the proton resonances would be found at much lower ppm values, in particular the signal due to the imine proton. The negative charge is thus probably localized dominantly on the metallic core, as also indicated by the much smaller ν(CO) wavenumbers of **2b** relative to those of $\mathbf{2}^{-\bullet}$ (see Table 2). The electron counting then implies that one of the Os–Os bonds in **2b** is broken, presumably the one between the o-^{i}Pr–PyCa-bridged Os atoms.

The reduction path of **2** is summarized in Scheme 2 which also shows the tentative molecular structure of **2b**. The molecular structures of **2** and **2b** presumably do not differ substantially, which may explain the aforementioned facile recovery of **2** on the back oxidation of **2b**. The fact that **2** was obtained with nearly 100% yield even in a bulk solution which was degassed prior to the

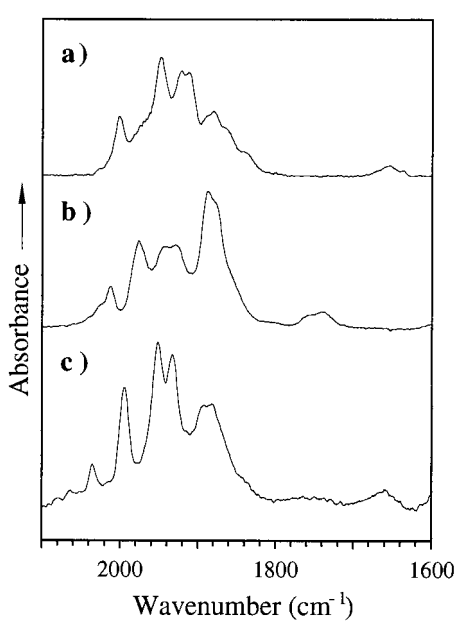

Fig. 6. IR spectra in the stretching carbonyl region: (a) **2b**, (b) **3c**, and (c) **4b**, all in THF. The spectra were obtained: (a) on reduction of $\mathbf{2}^{-\bullet}$ at 253 K; (b) on reduction of **3** at 293 K; (c) on reduction of $\mathbf{4}^{-\bullet}$ at 293 K, using OTTLE cells [18,19].

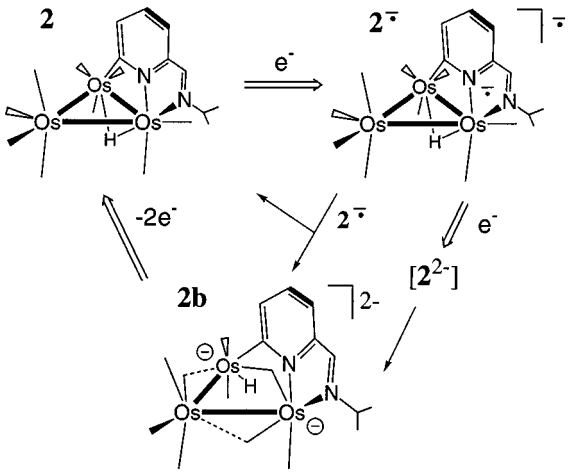

Scheme 2. The reduction path of the cluster **2**, with the tentative molecular structure of the dianion **2b** whose oxidation leads to the complete recovery of **2**.

oxidation of **2b** by a freeze-pump-thaw procedure, is a strong argument against reduction-induced CO dissociation from **2**. The latter reaction is known to take place during the two-electron reduction of $Os_3(CO)_{12}$ producing $[Os_3(CO)_{11}]^{2-}$ [9]. Unfortunately, the slow thermal decomposition of **2b** presents a serious obstacle for unambiguous determination of the molecular structure of **2b** from crystallographic and/or mass spectroscopic data.

3.3. Redox behaviour of $[HOs_3(CO)_9(6\text{-}CH_2\text{–}C_5H_3N\text{-}2\text{-}C(H)=N\text{–}^iPr)]$ (3)

The cyclic voltammogram of **3** in THF at 293 K and at $v = 100$ mV s^{-1} (see Fig. 7A) resembles that of **2**, showing the chemically reversible one-electron reduction at $E(R_1)$ and the chemically irreversible oxidation at $E(O_m)$. The radical anions $\mathbf{3}^{-\bullet}$ produced at $E(R_1)$ are further reduced irreversibly at $E(R_2)$. Differently from $\mathbf{2}^{-\bullet}$ (see Fig. 3), the reduction of $\mathbf{3}^{-\bullet}$ seems to consume more than one electron. Besides **3b** which is oxidized, similarly to **2b**, on the reverse scan at the potential $E(O_2')$, this intriguing cathodic step also yields another product, denoted as **3c**, which oxidizes at $E(O_2'')$. Notably, the oxidation of **3** at $E(O_m)$ turns at 220 K to a partly chemically reversible one-electron process. (see Fig. 7B).

The radical anion $\mathbf{3}^{-\bullet}$ was found to be less stable than $\mathbf{2}^{-\bullet}$. IR spectroelectrochemical experiments in THF at 253 K first showed the conversion of **3** at the cathodic potential $E(R_1)$ to $\mathbf{3}^{-\bullet}$ (see Table 2) which slowly decomposed already at the end of the reduction. Similarly to $\mathbf{2}^{-\bullet}$, the decomposition of $\mathbf{3}^{-\bullet}$ was much faster in more polar ^{n}PrCN and could not be inhibited even at 233 K. The two visible MLCT bands in the UV-vis spectrum of **3** shifted to shorter wavelengths for

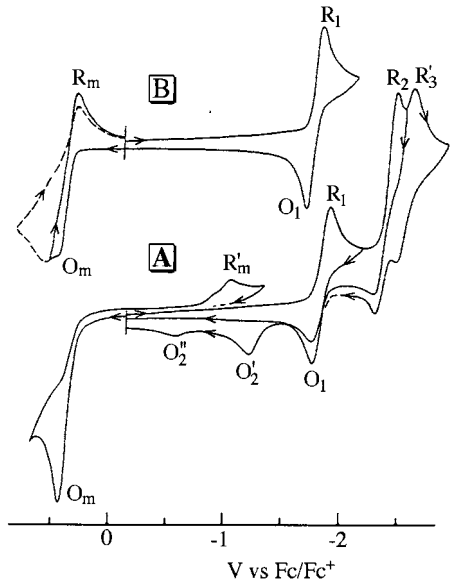

Fig. 7. Cyclic voltammograms of **3**. Conditions identical to Fig. 2A,B.

$\mathbf{3}^{-\bullet}$ (see Fig. 8 and Table 3), as might be anticipated for electronic transitions directed to the largely π^*(diimine)-localized LUMO of **3**, raised in energy by the single-electron occupation. The additional weak and broad absorption band of $\mathbf{3}^{-\bullet}$ at 877 nm may belong to intraligand (IL) transitions of the reduced *o*-^{i}Pr–PyCa{6-Me} ligand ([5]b). The poorly resolved EPR spectrum of $\mathbf{3}^{-\bullet}$ at $g = 1.9935$ (see Fig. 5b) does not substantially deviate from that of $\mathbf{2}^{-\bullet}$. The considerably smaller isotropic *g*-factor relative to that determined for $\mathbf{2}^{-\bullet}$ (see above), and also to the free-electron value $g_e = 2.0023$, may reflect a non-negligible contribution from one or more heavy Os atoms into the singly occupied MO (SOMO) of $\mathbf{3}^{-\bullet}$ due to intermixing with a nearby unoccupied MO.

Further reduction of $\mathbf{3}^{-\bullet}$ at R_2 and/or its thermal decomposition at R_1 (probably via disproportionation)

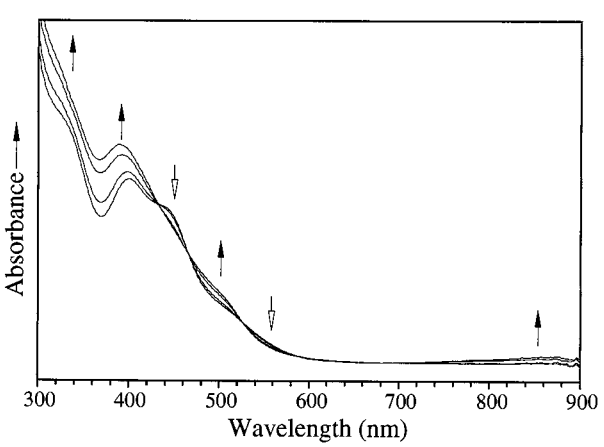

Fig. 8. UV-vis spectral changes during the reduction of **3** to $\mathbf{3}^{-\bullet}$. Conditions: THF, $T = 243$ K, in situ electrolysis within an OTTLE cell [19].

in the course of the spectroelectrochemical experiments in THF at 293–253 K only afforded the cluster **3c** which indeed oxidized, as was testified by thin-layer cyclic voltammograms, at the anodic potential $E(O_2')$ instead of $E(O_2')$ (see Fig. 7). The secondary product **3b**, oxidized in analogy with corresponding **2b** at $E(O_2')$ (see above), is apparently too short-lived to be detected on the spectroelectrochemical time scale of minutes. The IR spectrum of the product **3c** reveals some differences in the intensities of the ν(CO) bands and, in particular, much larger wavenumbers of the ν(CO) bands due to bridging carbonyl ligand(s), compared to the IR spectrum of the dianion **2b** (see Fig. 6a,b and Table 2). In addition, **3c** is thermally less thermally stable than **2b** both in THF and ^{n}PrCN. Future research should clarify the difference in the structure and stability between **2b** (see Scheme 1) and **3c**.

3.4. Molecular structure and redox behaviour of [$HOs_3(CO)_9$(2,3-dipyrid-2′-ylbenzoquinoxaline-14-yl)] (4)

Regardless of the close similarity between the α-diimine molecules 2,3-dipyrid-2-ylpyrazine (dpp) and 2,3-dipyridyl-2-ylbenzoquinoxaline (dpb) with two additional, cumulated aromatic rings, their reaction with $[Os_3(CO)_{10}(MeCN)_2]$ does not afford products with identical molecular structures, as was erroneously anticipated in a previous study ([5]a) The dpp ligand only coordinates to one Os atom as a σN,σN′-chelated four-electron donor. The IR spectrum of the product $[Os_3(CO)_{10}$(dpp)] shows the characteristic ν(CO) pattern observed for **1** (see Fig. 9a) and other $[Os_3(CO)_{10}$(α-diimine)] derivatives.[5] In contrast to this, the IR ν(CO) pattern of the dpb-containing triosmium cluster (see Fig. 9c) closely resembles that of the $[HOs_3(CO)_9(L)]$ clusters **2** and **3** (see Fig. 9b). In $[Os_3(CO)_{10}$(α-diimine)] the chelated dpb ligand is anticipated to exhibit a greater steric interference with a neighbouring $Os(CO)_4$ group as compared to the shorter dpp ligand. This interaction apparently activates a C–H bond of the benzoquinoxaline part and initiates the oxidative addition reaction producing the cluster $[HOs_3(CO)_{10}$(dpb-14-yl)] (**4**) (see Fig. 1d). An unambiguous evidence for the latter assignment was obtained from the ^{1}H-NMR spectra of **4** in CD_2Cl_2 and C_6D_6 (see Table 4) and the corresponding 2D COSY plots. In particular, it is evident that the dpb ligand in **4** only contains thirteen aromatic protons. The singlet signal for the dpb-proton H_{14} (see the numbering system as in Fig. 1d) was missing in the ^{1}H-NMR spectra, being replaced by the resonance at ca. −17.5 ppm due to a bridging hydride ligand [32]. These data clearly demonstrate that the σN,σN′-chelated dpb ligand is also attached to an adjacent Os centre through the C_{14} atom of the benzoquinoxaline moiety.

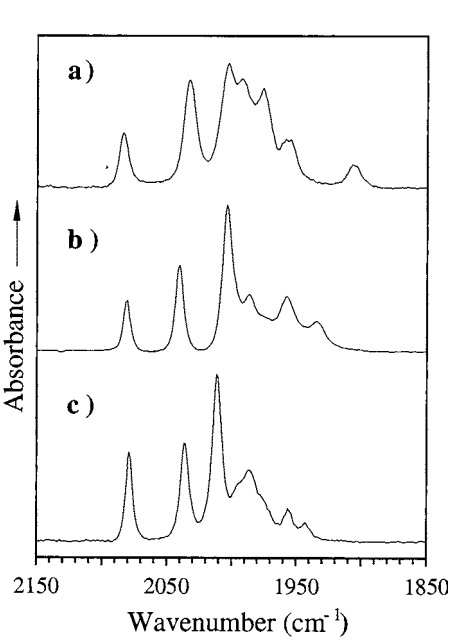

Fig. 9. IR spectra in the stretching carbonyl region: (a) **1**; (b) **2**; (c) **4**; all in THF at $T = 293$ K.

As expected, the cyclic voltammogram of **4** closely resembles that of the structurally related cluster **2**. In contrast to the nearly identical oxidation potentials $E(O_m)$ of **2** and **4**, the chemically and electrochemically reversible one-electron reduction of the latter cluster at $E(R_1)$ (293 K, $v = 20$ mV s^{-1}) occurs significantly more positively ($\Delta E_{1/2} = 460$ mV, see Table 1). This potential difference is attributed to a low energy of the LUMO of **4** possessing a dominant contribution from the lowest unoccupied π^* orbital of the strong π-accepting dpb-14-yl ligand. [33] The UV-vis spectrum of the inherently stable radical anion $\mathbf{4}^{-\bullet}$ indeed exhibits several absorption bands between 450 and 750 nm (see Fig. 10 and Table 3) belonging to intraligand (IL) $\pi^* \rightarrow \pi^*$ transitions of the [dpb-14-yl]$^{-\bullet}$ ligand, which are also found in the UV-vis spectrum of uncoordinated [dpb]$^{-\bullet}$ (see the inset to Fig. 10 and Table 3). The low-energy electronic transitions of $\mathbf{4}^{-\bullet}$ at $\lambda_{max} = 819$ nm and above 900 nm have no equivalents in the UV-vis spectrum of uncoordinated [dpb]$^{-\bullet}$. They may correspond to additional IL transitions of the *ortho*-metallated [dpb-14-yl]$^{-\bullet}$ ligand, though this possibility was not further investigated. The broad lowest-energy absorption band of **4** at 694 nm, encompassing at least two MLCT transitions, shifted, as expected, to a higher energy on the one-electron reduction and became obscured by the IL bands of $\mathbf{4}^{-\bullet}$ at 510 and 566 nm.

The EPR spectrum of $\mathbf{4}^{-\bullet}$ at $g = 2.0021$ (see Fig. 5c) documents that the unresolved hyperfine structure is a common feature of all the radical anions $[HOs_3(CO)_9(L)]^{-\bullet}$ under study. The only apparent difference concerns the relatively large deviation of the isotropic g-factors from the free-electron value g_e

Table 4
Solvent dependence of the ^{1}H-NMR[a] data of [(μ-H)$Os_3(CO)_{10}$(2,3-dipyrid-2′-ylbenzoquinoxaline-14-yl)] (**4**) at 293 K

^{1}H nucleus[b]	C_6D_6		CD_2Cl_2		Δ[c]
	δ (ppm)	J(H,H) (Hz)	δ (ppm)	J(H,H) (Hz)	
3′	7.82 d	7.90	8.17 d	7.69	0.35
4′	7.09 (td)[d]		8.05 td[e]	7.77/1.39	0.96
5′	6.51 dd	7.12/4.9 7	7.49 t[e]	6.15	0.98
6′	8.00 d	4.84	8.60 d	4.67	0.60
3″	6.60 d	8.31	7.18 d	8.46	0.58
4″	6.27 td	7.52/1.03	7.53 td[e]	8.01/1.20	1.26
5″	6.02 t	6.07	7.36 t	6.07	1.34
6″	8.62 d	5.67	9.39 d	5.53	0.77
7	8.52 s		8.52 s		0
9	9.26 d	9.13	9.10 d	9.20	−0.16
10	7.48 td	8.37/1.29	7.82 td	8.36/1.20	0.24
11	7.12 (t)[d]		7.61 t	7.25	0.49
12	7.66 d	8.09	8.09 d[e]	7.83	0.33
14	−17.61 s		−17.46 s		−0.15

[a] 300.11 MHz.
[b] ***3′–6′***: uncoordinated pyridyl ring of dpb; ***3″–6″***: Os-coordinated pyridyl ring of dpb; ***7***, ***9–12***: benzoquinoxaline moiety; ***14***: Os–Os-bridging hydride atom, originally at C_{14} of the uncoordinated dpb ligand (see Fig. 1d).
[c] $\Delta = \delta(CD_2Cl_2) - \delta(C_6D_6)$.
[d] Obscured by C_6D_6 signal; chemical shifts determined from the 2D COSY plot.
[e] The signals of the protons ***4′***/***12*** and ***4″***/***5′*** in CD_2Cl_2 partly overlap (multiplets); chemical shifts correspond with those obtained from the 2D COSY diagram.

($\Delta g_{iso} = g - g_e$) for $\mathbf{2}^{-\bullet}$ and $\mathbf{3}^{-\bullet}$ (see above) in contrast to $\Delta g_{iso} \sim 0$ for $\mathbf{4}^{-\bullet}$. These parameters may reflect variable degree of spin-orbit coupling and intermixing between the SOMO of these radical anions and (un)occupied MOs in its proximity. The difference between the Δg_{iso} values can indeed still be large even if the contribution of Os to the SOMO by way of spin polarization [34] is not significantly altered, taking into account the large spin-orbit coupling constant ζ(Os) ~ 3000 cm^{-1} [35] to which Δg_{iso} is directly proportional [36]. The nearly zero Δg_{iso} for $\mathbf{4}^{-\bullet}$ points to almost exclusive localization of the odd electron on the π^* SOMO of the aromatic [dpb-14-yl]$^{-\bullet}$ ligand.

Subsequent one-electron reduction of $\mathbf{4}^{-\bullet}$ (see Table 1) was found to be only partly chemically reversible at moderate cyclic voltammetric scan rates, as reflected in $I_{p,a}/I_{p,c} = 0.57$ at $v = 100$ mV s^{-1} (THF, 293 K). Instead of unsstable $\mathbf{4}^{2-}$, this step afforded a product **4b** whose IR spectrum is close to that of **2b**, in particular due to the presence of the weak ν(CO) band at 1664 cm^{-1} in the bridging carbonyl region, but also resembles that of **3c** (see Fig. 6 and Table 2). This result points to identical secondary reactions of the transients $\mathbf{2}^{2-}$ and $\mathbf{4}^{2-}$, as depicted for $\mathbf{2}^{2-}$ in Scheme 1.

3.5. Molecular orbital calculations

Extended Hückel MO calculations were performed on the *ortho*-metallated clusters **2** and **3**, and on a model of **1** (see Section 2) in order (i) to find the positions of the bridging hydride ligands in **2** and **3**, which could not be located unequivocally from crystal data [14,15], (ii) to study the bonding of the diimine ligand to the cluster, and (iii) to compare the frontier orbitals of **1**–**3** with regard to the different redox behaviour of these clusters, in particular to the higher stability of the radical anions $\mathbf{2}^{-\bullet}$ and $\mathbf{3}^{-\bullet}$ in comparison with $\mathbf{1}^{-\bullet}$ (see above).

Extended Hückel calculations indeed proved to be useful for location of edge- and/or face-bridging hy-

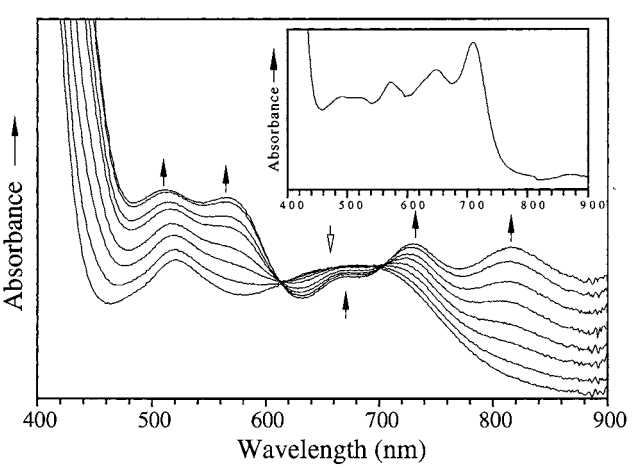

Fig. 10. UV-vis spectral changes during the reduction of **4** to $\mathbf{4}^{-\bullet}$. Conditions: THF, $T = 293$ K, in situ electrolysis within an OTTLE cell [18]. Inset: UV-vis spectrum of [dpb]$^{-\bullet}$ recorded under the same conditions.

dride ligands in metal cluster carbonyls [37]. Herein, the same method was employed as previously calibrated for $[HRu_3(CO)_9(\mu_3\text{-}\eta^3\text{-}C_4H_5]$ [38]. For both **2** and **3** Zoet et al. assumed the hydride bridging between the $Os_{(2)}$–$Os_{(3)}$ atoms as numbered in Fig. 1, below the Os_3 plane opposite to the bridging terdentate diimine ligand [14,15]. The relative energies calculated for the possible isomers of **2** and **3**, respectively, are as follows: in-plane hydride bridging along (a) the $Os_{(2)}$–$Os_{(3)}$ bond: 0.45 and 0.0 eV, (b) the $Os_{(1)}$–$Os_{(2)}$ bond: 0.40 and 0.98 eV, (c) $Os_{(1)}$–$Os_{(3)}$ bond: 1.01 and 1.22 eV; (d) face-capping hydride: 0.0 and 0.13 eV. The possibility suggested by Zoet et al. was also tested and gave an energy in between those found for the hydride positions (a) and (d). These data suggest that the most stable structure for **2** presents the face-capping hydride ligand, while for **3** a facile interconversion between the $Os_{(2)}$–$Os_{(3)}$ edge-bridging and face-capping structures is most probable. This result is reflected in the larger total Os–H overlap population (0.60 for **2** and 0.55 for **3**). We therefore anticipate that the hydride ligand in **2** is more firmly bound than that in **3**, which also might explain the higher stability of the corresponding radical anion $\mathbf{2}^{-\bullet}$ (see above).

The diimine ligand in the cluster **2** binds to the metal core through the three lone pairs on the two nitrogen atoms and the carbon atom (σ_1, σ_2, σ_3), which donate electrons to three empty orbitals of the cluster fragment, as shown schematically in Fig. 11. Indeed, as there is no symmetry, all levels mix. There is significant backdonation to the lowest energy π^* orbital of the diimine ligand, with large contributions from the nitrogen atoms and smaller from the carbon atom binding to the metal core. As a consequence, the ligand is very strongly bound to the osmium atoms, as compared to the cluster **1** where only two Os–N bonds are formed (the bonding scheme is similar, with significant backdonation only to the first π^* orbital, a butadiene-type orbital largely localized on the nitrogen atoms).

The frontier orbitals of **1**–**3** are depicted and described in Fig. 12. The origin of the HOMO and the LUMO is comparable for the three clusters. We are aware of the limitations of the EHMO method, which are more apparent in the energies than in the characters of the HOMO and LUMO, when comparing them with those from density functional calculations [39]. Though the energies differ significantly, the characters are comparable, so that some comparisons can be drawn. (i) Most importantly, the LUMO of **2** and **3** is clearly more localized on the α-diimine ligand than calculated in the case of **1**. This difference probably explains the higher stability of the radical anions derived from **2** and **3**. For, the single occupation of their LUMO will destabilize less the bonding within the (μ-H)Os_3 core. (ii) The ligand-cluster binding energy, defined as the difference between the energy of the

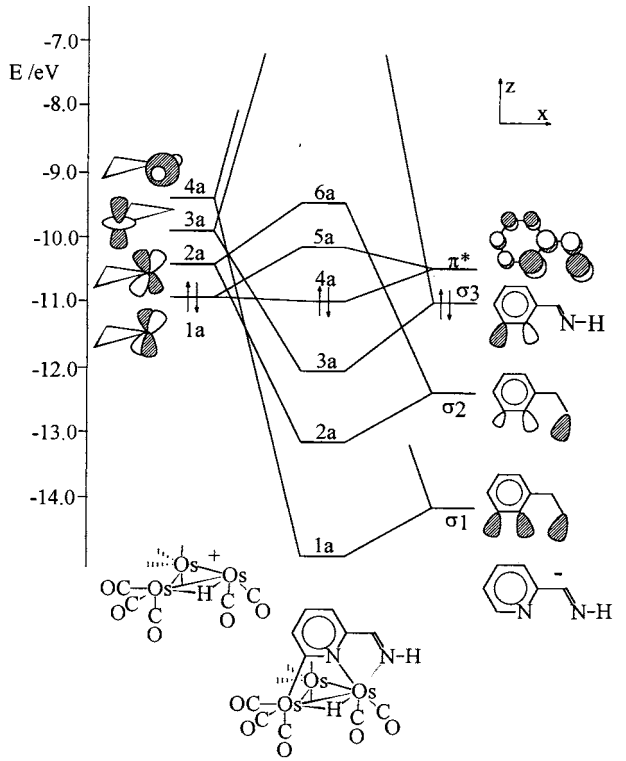

Fig. 11. Interaction diagram between the $Os_3(CO)_9H^+$ fragment (left side) and the diimine ligand (right side) in the cluster **2**. The four CO ligands at the Os_3 atom have been omitted for clarity.

cluster and the sum of the energies of the diimine ligand and the Os_3-containing fragment, decreases from 2.54 to 2.36 eV for **1** when the cluster is reduced with one electron, from 5.71 to 5.61 eV for **2**, and from 4.63 to 4.55 eV for **3**, respectively. These values also indicate that the stability of the cluster **1** is more affected by the reduction than that of the others. (iii) The EH calculations confirm the aforementioned dominant MLCT character of the lowest electronic transition in **1**–**3**, though the theoretical HOMO-LUMO gap (0.5–1 eV) is much smaller than that derived from the redox potentials and electronic absorption spectra (2–2.5 eV). It should be recalled that the latter spectra were of course not obtained in vacuum. (iv) The higher energies of the HOMO ($\Delta E = 0.13$ eV) and the LUMO ($\Delta E =$ 0.11 eV) for **3** in comparison with **2** nicely correspond with the lower oxidation and reduction potentials of the former cluster (see Table 1). The higher energies of the frontier orbitals in the case of **3** might be ascribed to a destabilizing σ-donor effect of the methylene group on the pyridine ring of the *ortho*-metallated ^{i}Pr–PyCa{6-Me} ligand, or to the different coordination geometry of the diimine. Indeed, the ligand-core overlap populations are 1.05 for **2** and 0.89 for **3**. Apart from the less firmly bound hydride ligand in **3** (see above), the latter property may also contribute to the experimentally observed lower stability of the radical anion $\mathbf{3}^{-\bullet}$ in

comparison with $\mathbf{2}^{-\bullet}$. The present data, however, do not provide a clue to the observed higher stability of the radical cation $\mathbf{3}^{+\bullet}$, detectable by cyclic voltammetry at low temperatures.

4. Conclusions

The presence of bridging *ortho*-metallated α-diimine ligands in the clusters $[HOs_3(CO)_9(L)]$ (L = *o*-^{i}Pr–PyCa (**2**), *o*-^{i}Pr–PyCa{6-Me} (**3**)) results in a remarkable stabilization with regard to the Os–Os bond cleavage upon one-electron reduction. The latter reaction is a characteristic feature of the reduction path of the clusters $[Os_3(CO)_{10}(\alpha\text{-diimine})]$ with a strong σ-donor α-diimine ligand represented herein by σN,σN′-chelated ^{i}Pr–PyCa (**1**). The radical anions $\mathbf{2}^{-\bullet}$ and $\mathbf{3}^{-\bullet}$ owe their much higher stability compared to $\mathbf{1}^{-\bullet}$ mainly to the higher cluster-diimine binding energy and to larger localization of the odd electron in the π^*(α-diimine) orbital, as evident from the EH-MO calculations. The inherent stability of the radical anion $[HOs_3(CO)_9(dbp\text{-}14\text{-}yl)]^{-\bullet}$ ($\mathbf{4}^{-\bullet}$) then reflects both the stabilizing factor of the *ortho*-metallated structure and the much larger p-acceptor capacity of the dpb molecule relative to that of ^{i}Pr–PyCa{6-X} (X = H, Me).

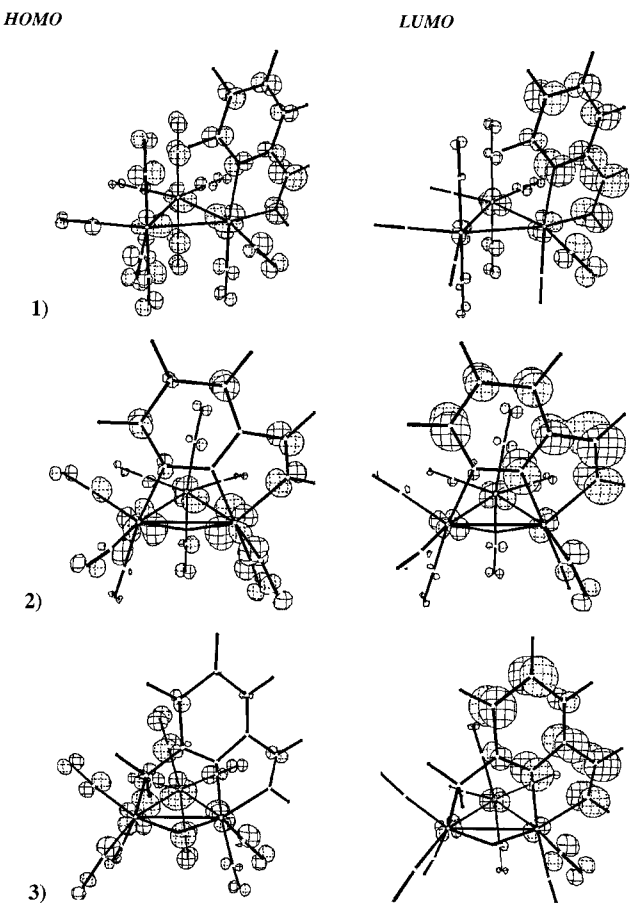

Fig. 12. Three-dimensional representation of the frontier orbitals of **1-3**, derived from extended Hückel calculations (see Section 2 for details). Orbital composition (energy in eV): **1** HOMO-79% cluster core, 21% π^* ^{i}Pr–PyCa (−10.84), LUMO-31% cluster core, 69% π^* ^{i}Pr–PyCa (−10.36 eV); **2** HOMO-89% cluster core, 11% *o*-^{i}Pr–PyCa (7% π^*) (−11.02), LUMO-23% cluster core, 77% π^* *o*-^{i}Pr–PyCa (−10.04); **3** HOMO-94% cluster core, 6% *o*-^{i}Pr–PyCa{6-Me} (4% π^*) (−10.89), LUMO-18% cluster core, 82% π^* *o*-^{i}Pr–PyCa{6-Me} (−9.93 eV).

Acknowledgements

The Netherlands Foundation for Chemical Research (SON), the Netherlands Organization for Scientific Research (NWO), Junta Nacional de Investigação Científica e Technológica (Portugal), and the TMR network *Metal Clusters in Catalysis and Organic Synthesis* are acknowledged for financial support. We also thank Professor S. Aime, Dr E. Valls (both University of Turin), Dr E. Hunstock (ITQB, Oeiras, Portugal) and Mr. M.J. Bakker (University of Amsterdam) for providing us with some unpublished experimental results.

References

[1] M.G. Richmond, Coord. Chem. Rev. 160 (1997) 237.
[2] (a) N.E. Leadbeater, J. Chem. Soc., Dalton Trans. (1995) 2923. (b) J.A. Krause, U. Siriwardane, T.A. Salupo, J.R. Wermer, D.W. Knoeppel, S.G. Shore, J. Organomet. Chem. 454 (1993) 263.
[3] F.-S. Kong, W.-T. Wong, J. Chem. Soc., Dalton Trans. (1997) 1237, and references therein.
[4] (a) R. Uson, L.A. Oro, M.T. Pinillos, M. Royo, E. Pastor, J. Mol. Catal. 14 (1982) 375. (b) P. Kalck, A. Thorez, M.T. Pinillos, L.A. Oro, J. Mol. Catal. 31 (1985) 311.
[5] (a) J.W.M. van Outersterp, M.T. Garriga Oostenbrink, H.A. Niewenhuis, D.J. Stufkens, F. Hartl, Inorg. Chem. 34 (1995) 6312. (b) J. Nijhoff, M.J. Bakker, F. Hartl, D.J. Stufkens, W.-F. Fu, R. van Eldik, Inorg. Chem. 37 (1998) 661.
[6] F.Hartl, J.W.M. van Outersterp, D.J. Stufkens, Organometallics, submitted.
[7] (a) T. van der Graaf, D.J. Stufkens, A. Oskam, K. Goubitz, Inorg. Chem. 30 (1991) 599. (b) T. van der Graaf, R.M.J. Hofstra, P.G.M. Schilder, M. Rijkhoff, D.J. Stufkens, J.G.M. van der Linden, Organometallics 10 (1991) 3688.
[8] B.D. Rossenaar, F. Hartl, D.J. Stufkens, C. Amatore, E. Maisonhaute, J.-N. Verpeaux, Organometallics 16 (1997) 4675.
[9] A.J. Downard, B.H. Robinson, J. Simpson, A. Bond, J. Organomet. Chem. 320 (1987) 363.
[10] D. Astruc, J.-R. Hamon, M. Lacoste, M.-H. Desbois, E. Román, in: R.B. King (Ed.), Organometallic Synthesis, vol. IV, Elsevier, Amsterdam, 1988, p. 172.
[11] H. Bock, H. tom Dieck, Chem. Ber. 100 (1967) 228.
[12] (a) G.Z. Bähr, H. Thämlitz, Z. Anorg. Allg. Chem. 282 (1955) 282. (b) Ibid., 292 (1957) 119. (c) A. Robinson, J.D. Curry, D.H. Busch, Inorg. Chem. 6 (1963) 1178.
[13] J.A. Baiano, D.L. Carlson, G.M. Wolosh, D.E. DeJesus, C.F. Knowles, E.G. Szabo, W.R. Murphy, Inorg. Chem. 29 (1990) 2327.

[14] R. Zoet, G. van Koten, K. Vrieze, A.J.M. Duisenberg, A.L. Speck, Inorg. Chim. Acta 148 (1988) 71.
[15] R. Zoet, G. van Koten, K. Vrieze, J. Jansen, K. Goubitz, C.H. Stam, Organometallics 7 (1988) 1565.
[16] G. Gritzner, J. Kuta, Pure Appl. Chem. 56 (1984) 461.
[17] C. Amatore, M. Azabi, P. Calas, A. Jutand, C. Lefrou, Y. Rollin, J. Electroanal. Chem. Interfacial Electrochem. 288 (1990) 45.
[18] M. Krejčík, M. Daněk, F. Hartl, J. Electroanal. Chem, Interfacial Electrochem. 317 (1991) 179.
[19] F. Hartl, H. Luyten, H.A. Nieuwenhuis, G.C. Schoemaker, Appl. Spectrosc. 48 (1994) 1522.
[20] R.D. Allendoerfer, G.A. Martinchek, S. Bruckenstein, Anal. Chem. 47 (1975) 890.
[21] F. Hartl, unpublished work.
[22] (a) R. Hoffmann, J. Chem. Phys. 39 (1963) 1397. (b) R. Hoffmann, W.N. Lipscomb, J. Chem. Phys. 36 (1962) 2179.
[23] J.H. Ammeter, H.-B. Bürgi, J.C. Thibeault, R. Hoffmann, J. Am. Chem. Soc. 100 (1978) 3686.
[24] C. Mealli, D.M. Proserpio, J. Chem. Educ. 67 (1990) 39.
[25] R. Zoet, J.T.B.H. Jastrzebski, G. van Koten, T. Mahabiersing, K. Vrieze, D. Heijdenrijk, C.H. Stam, Organometallics 7 (1988) 2108.
[26] E. Hunstock, ITQB, personal communication.
[27] N.E. Leadbeater, J. Lewis, P.R. Raithby, G.N. Ward, J. Chem. Soc., Dalton Trans. (1997) 2511.
[28] G.J. Stor, F. Hartl, J.W.M. van Outersterp, D.J. Stufkens, Organometallics 14 (1995) 1115.
[29] The zwitterion **1a**·CO was generated as a stable photoproduct on visible irradiation of **1** in CO-saturated THF at 213 K. The solvent-stabilized zwitterion **1a**·THF reacted under the same conditions to give back parent **1**. M.J. Bakker, University of Amsterdam, unpublished results.
[30] (a) K.E. Inkrott, S.G. Shore, Inorg. Chem. 18 (1979) 2817. (b) D. Osella, C. Nervi, M. Ravera, J. Fiedler, V.V. Strelets, Organometallics 14 (1995) 2501.
[31] (a) ^{1}H-NMR spectrum of **2** (300.11 MHz, THF-d_8): δ (ppm) 8.36 (s, 1H, imine H); 7.47–7.36 (m, 3H; pyridyl H); 4.43 (sept, ^3J(H,H) = 6.5 Hz, 1H, $(CH_3)_2CH$); 1.61 (d, ^3J(H,H) = 6.5 Hz, 3H, $(CH_3)_2CH$); 1.56 (d, ^3J(H,H) = 6.5 Hz, 3H, $(CH_3)_2CH$); −20.43 (s, 1H, hydride bridge). The ppm values, in particular that for the signal of the imine proton, significantly deviate in comparison with the ^{1}H-NMR spectrum of **2** in C_6D_6 [14]. (b) ^{1}H-NMR spectrum of **2b** (300.11 MHz, THF-d_8): δ (ppm) 8.73 (s, 1H, imine H); 7.18 (d, ^3J(H,H) = 7.5 Hz, 1H, pyridyl H); 7.16 (d, ^3J(H,H) = 7.5 Hz, 1H, pyridyl H); 6.71 (t, ^3J(H,H) = 7.5 Hz, 1 H, pyridyl H); 3.61 (sept, ^3J(H,H) = 6.5 Hz, 1H, $(CH_3)_2CH$); 1.20 (d, ^3J(H,H) = 6.5 Hz, 6H, $(CH_3)_2CH$); −11.66 (s, 1H, terminal hydride).
[32] (a) A.P. Humphries, H.D. Kaesz, Progr.Inorg.Chem. 25 (1975) 145. (b) In ^{1}H-NMR spectra of five isomeric [H(μ-H)$Os_3(CO)_{10}(PHEt_2)$] clusters the proton resonance due to the terminal hydride ligand occurs at ca. −10.0 ppm while the signal due to the edge-bridging hydride ligand was found at ca. −20.0 ppm. S. Aime, R. Gobetto, E. Valls, Inorg. Chim. Acta 275–276 (1998) 521.
[33] It should be recalled that the same trend has been reported for the complexes [Re(X)$(CO)_3$(α-diimine), X = Br, α-diimine = ^{i}Pr-PyCa ($E_{1/2}$ = −1.70 V versus Fc/Fc$^+$ (in THF)) [27] and X = Cl, α-diimine = dpb ($E_{1/2}$ = −0.54 V versus Ag/AgCl = ∼ −1.0 V versus Fc/Fc$^+$ (in MeCN) [13]. The LUMO of these complexes possesses a dominant π^* (α-diimine) character.
[34] W. Kaim, Coord. Chem. Rev. 76 (1987) 187.
[35] T.J. Meyer, Pure Appl. Chem. 58 (1986) 1193.
[36] $\Delta g_{iso} = g - g_e = g - 2.0023 = k\zeta(1/\Delta E_1 - 1/\Delta E_2)$, where ΔE_1 and ΔE_2 are the energy differences between the SOMO and the HOMO and LUMO, respectively. For example see Ref. [32], and P.S. Braterman, J.-I. Song, C. Vogler, W. Kaim, Inorg. Chem. 32 (1992) 222.
[37] R. Hoffmann, B.E.R. Schilling, R. Bau, H.D. Kaesz, D.M.P. Mingos, J. Am. Chem. Soc. 100 (1978) 6088.
[38] D. Braga, F. Grepioni, D.B. Brown, B.F.G. Johnson, M.J. Calhorda, L.F. Veiros, J. Chem. Soc., Dalton Trans. (1997) 547.
[39] According to the density functional calculations [26], the cluster [$Os_3(CO)_{10}$(H-PyCa)], the model derivative of **1**, possesses the HOMO (−5.39 eV) and the LUMO (−3.89 eV) localized for 28 and 65%, respectively, on the H–PyCa ligand.